Soft Matter

PAPER

How nanorough is rough enough to make a surface superhydrophobic during water condensation?

Konrad Rykaczewski,[*a] William A. Osborn,[a] Jeff Chinn,[b] Marlon L. Walker,[a] John Henry J. Scott,[a] Wanda Jones,[b] Chonglei Hao,[c] Shuhuai Yao[d] and Zuankai Wang[c]

Nanostructured surfaces which manifest superhydrophobic properties during water condensation have a potential to dramatically enhance energy efficiency in power generation and desalination systems. Although various such surfaces have been reported, their development has been fortuitous, not driven by an understanding of the underlying physical processes. In this work, we perform a comprehensive study of microscale water condensation dynamics on nanostructured superhydrophobic surfaces made using a variety of synthetic methods. We demonstrate that the growth mechanism of individual water microdroplets on these surfaces is universal and independent of the surface architecture. The key role of the nanoscale topography is confinement of the base area of forming droplets, which allows droplets to grow only through contact angle increase. The nearly spherical droplets formed in this fashion become highly mobile after coalescence. By comparing experimentally observed drop growth with interface free energy calculations, we show that the minimum observed confined microdroplet base diameter depends directly on the nanoscale surface roughness and degree of interfacial wetting. Specifically, we show that the microscale condensation mechanism depends on the height of a liquid film with volume equal to the fill volume between the nanostructures. This introduced roughness length scale is a universal metric that allows for facile comparison of arbitrarily complex surface architectures. We use this new fundamental insight to develop quantitative design guidelines for superhydrophobic surfaces intended for condensation applications.

Introduction

Surfaces which manifest superhydrophobic properties during water condensation have a potential to dramatically enhance energy efficiency in power generation[1] and desalination[2] systems. The use of these coatings is predicted to significantly increase the heat transfer rate during dropwise condensation[1] by promoting the formation of nearly spherical microscale droplets, which become highly mobile as a result of coalescence events.[3–6] The surface architecture length scale has proven to be the crucial parameter in designing superhydrophobic coatings for dropwise condensation. Specifically, coatings with microscale features and a macroscale water contact angle above 150° either wet completely during condensation or have a wetting behavior similar to flat hydrophobic surfaces.[7–20] However, a few natural[21–23] and artificial[1,3,4,6,24–33] nanostructured superhydrophobic surfaces retain their superhydrophobic characteristics during water condensation. Thus far, the development of such "properly designed" nanostructured superhydrophobic surfaces has been fortuitous, not driven by an understanding of the underlying physical processes.[34] In this work we examine the role of nanoscale surface roughness in the mechanism of individual droplet formation. We use *in situ* Environmental Scanning Electron Microscopy™ (ESEM™) (ref. 35) † and light microscopy to study water condensation dynamics on surfaces with nanoscale roughness and macroscale water contact angles in the range of ≈100° to ≈165°. The nanostructured surfaces are made using a variety of synthetic techniques, including nanoparticle vapor deposition,[5,29,36] vapor–liquid–solid (VLS) catalytic growth,[37] Deep Reactive Ion Etching (DRIE),[37] and Metal-assisted Chemical Etching (MaCE) of silicon.[38–42] All surfaces are modified with a thin hydrophobic coating (see Experimental

[a]*Material Measurement Laboratory, National Institute of Standards and Technology, Gaithersburg, MD 20899, USA. E-mail: konrad.rykaczewski@nist.gov*

[b]*Integrated Surface Technologies, Inc., 1455 Adams Dr., Ste 1125, Menlo Park, CA 94025, USA*

[c]*Department of Mechanical and Biomedical Engineering, City University of Hong Kong, Hong Kong, China*

[d]*Department of Mechanical Engineering, Hong Kong University of Science and Technology, Hong Kong, China*

† Certain commercial equipment, instruments, and materials are identified in this publication to adequately specify the experimental procedure. Such identification in no way implies approval, recommendation, or endorsement by NIST, nor does it imply that the equipment, instruments, or materials identified are necessarily the best available for the purpose.

section for details). By comparing experimentally observed drop growth with interface free energy (IFE) calculations, we show that the observed minimum confined microdroplet base diameter is directly linked to the nanoscale surface roughness length scale and the degree of interfacial wetting. We also experimentally correlate the individual droplet growth mechanism to the mobility of drops after coalescence. We use our new fundamental insight to develop quantitative design guidelines for superhydrophobic surfaces intended for condensation applications.

Results and discussion

To begin growing on any surface, nucleated droplets must have the radius of curvature, r,[43] greater than the critical radius, $r_{min} = 2T_{sat}\sigma_{lg}/H_{fg}\rho_l\Delta T$ [where T_{sat} is the vapor saturation temperature, σ_{lg} is the liquid water surface tension, H_{fg} is the latent heat of vaporization of water, ρ_l is the liquid density, and $\Delta T = T_{sat} - T_{surf}$ is the temperature difference between the vapor and the solid surface, which is also referred to as surface subcooling]. Depending on the level of surface subcooling, the value of r_{min} varies from a few nanometers to a few hundred nanometers. If the topographical features of a hydrophobic surface have the width, l, or spacing, L, much larger than the critical radius ($l \gg r_{min}$ and/or $L \gg r_{min}$), condensing drops initially grow in the same fashion as on a flat surface and later proceed to bridge and fill in the microscale gaps.[7–20,44] Our experimental observations demonstrate that the converse scaling, $r_{min} \gg l$ and/or $r_{min} \gg L$, is not a necessary condition for a surface to be superhydrophobic during water condensation. Specifically, we observe formation of nearly spherical microdroplets on surfaces with l and L ranging from tens of nanometers to hundreds of nanometers and environmental conditions corresponding to r_{min} in the range of 3 nm to 830 nm.‡ Therefore, in the case $r_{min} \sim l$ and/or $r_{min} \sim L$, simple scaling arguments do not predict the wetting properties of superhydrophobic surfaces and the droplet growth mechanism needs to be assessed further.

We found that on surfaces which evince superhydrophobic characteristics during water condensation, the growth mechanism for individual droplets is universal and does not depend on the type of surface nanoscale topography. Specifically, droplet growth begins when a nucleated liquid bridges surface asperities to form a horizontal interface. Merging of neighboring water nanodroplets leads to the formation of a wetted flat spot with a base area of a few square micrometers.[27,28] Confinement of the base area allows the droplet to grow only through contact angle increase.[5,27,28,33] Here we note that even at this stage the condensed liquid can be in a fully wetting Wenzel[45] or partially wetting Cassie–Baxter state.[32,46,47] After the droplet reaches a contact angle of 130° to 150° its base diameter increases in discrete steps with periods of purely confined base area growth in-between.[33] An example of the constant base area growth mode is illustrated in the sequence of ESEM™ images in Fig. 1a. In this case the microdroplet growth occurs on an alumina nanoparticle coating created through six cycles of trimethylaluminium and water vapor injection, followed by the
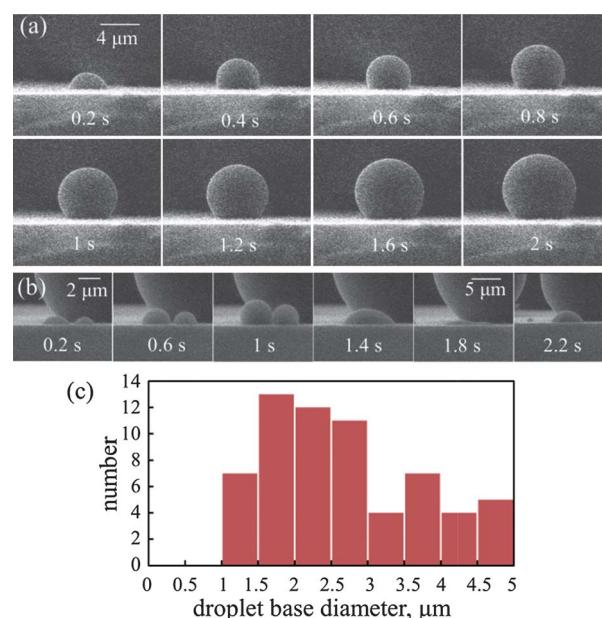
Fig. 1 Sequence of 90° ESEM™ images illustrating (a) the nearly constant base area growth of an isolated droplet, (b) the wetting history dependent constant base area growth, and (c) the resulting droplet base diameter size distribution below 5 μm for condensation on the 6 NP surface.

deposition of an encapsulating silica matrix (referred to as the 6 NP surface). We observed that on all the examined surfaces the value of the initial confined base diameter, d_{base}, varies significantly from drop to drop. The histogram in Fig. 1c illustrates that on the 6 NP surface we observed constant base area growth of droplets with d_{base} ranging from 1 μm to 5 μm (larger base diameters were also observed but are not analyzed in this work). Our experiments also suggest that d_{base} is dependent on the wetting history of each specific location on the surface. In particular, the series of ESEM™ images in Fig. 1b is a demonstration of sequential constant base area growth of drops with $d_{base} \approx 5$ μm from a preferential nucleation site that was formed after coalescence of two smaller drops with $d_{base} \approx 2.5$ μm. To begin with, the contact angle of the new drop is much lower than 90° but then increases until the drop comes in contact with the significantly larger background drop. This large primary drop does not cover the nucleation site during coalescence, allowing for condensation of multiple droplets on the same site.[5] A possible explanation for the formation of these preferred nucleation areas is that after coalescence with larger drops[5] the base area of the drop is not fully dried. In this case, condensation will preferentially occur[48] on the thin film of water left over after a coalescence event, which has a significantly lower surface energy than the surrounding substrate.

So how does the nanoscale surface architecture confine the base diameter of forming droplets? To answer this question we examine the relation between possible wetted flat spot growth modes and surface topography. The schematic in Fig. 2 illustrates that the flat wetted spot can grow by either expanding horizontally across the nanostructures or increasing its contact angle. From a thermodynamic perspective, the liquid will expand in a fashion that minimizes its IFE.[49–51] To determine which growth mode is favorable, we calculate the IFE for a flat wetted spot with the initial projected
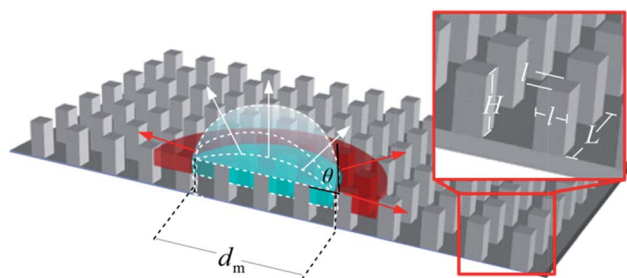
Fig. 2 Schematic of a liquid filling a volume between nanostructures, forming a flat circular wetted spot with the base area, A_{base}, and corresponding base diameter, d_m. This liquid can either expand horizontally by filling up more volume between the nanostructures or by increasing its contact angle and forming a drop. The inset shows a detailed schematic of a hypothetical periodic square pillar topography with height H, width l, and spacing L.

base area, A_{base}, formed between nanostructures with arbitrary geometry. We define the area roughness parameters, R_a, as the total surface area of the nanostructures, A_{total}, divided by A_{base}. We also define a volumetric roughness parameter, R_v, as the volume of condensed liquid completely filling the voids between the nanostructures, V_{total}, divided by A_{base}. R_v is a roughness length scale that represents the thickness of a liquid film with volume equal to V_{total} and thus will be referred to as the equivalent film height. Taking into consideration the possibility of the condensed liquid being in the Cassie–Baxter state, we also define f as the ratio of wetted surface area, A_{wet}, to A_{total}, and F as the ratio of volume of the condensed liquid partially filling the voids between the nanostructures, V_{wet}, to V_{total}. Both the top and the bottom liquid–air interfaces of the wetted flat spot are assumed to be horizontal.[46,49] If the fluid expands by increasing its contact angle from zero to θ, the initial volume of the wetted flat spot, $V_{wet} = A_{base}R_vF$, increases by $V_{cap} = \pi(4A_{base}/\pi)^{2/3}(2 + \cos \theta)(1 - \cos \theta)^2/(24 \sin^3 \theta)$.[35] For a fluid expanding horizontally with a circular base, the equivalent volume rise would increase the base area to A_n:

$$A_n = A_{base} + \frac{(4A_{base})^{2/3}(2 + \cos \theta)(1 - \cos \theta)^2}{24\pi^{1/2}FR_v\sin^3 \theta} \quad (1)$$

For a liquid of any shape condensed on the nanostructures, the IFE is equal to:

$$E = A_{lg}\sigma_{lg} + A_{ls}\sigma_{ls} + A_{sg}\sigma_{sg} \quad (2)$$

where A_{lg}, A_{ls}, σ_{ls}, A_{sg} and σ_{sg} are the gas–liquid interfacial area, the liquid–solid interfacial area and surface tension, and the solid–gas interfacial area and surface tension, respectively. In particular, the IFE for the expanded flat wetted spot, E_{SPOT}, is equal to:

$$E_{SPOT} = \sigma_{lg}A_n(2 - f) + \sigma_{ls}A_nR_af + \sigma_{sg}A_nR_a(1 - f) \quad (3)$$

To calculate the IFE for growth through contact angle increase, E_{CA}, we also take into account the solid–gas interfacial area which is covered by the expanded but not the initial wetted spot, $(A_n - A_{base})R_a$. Specifically,

$$E_{CA} = \sigma_{lg}(A_{cap} + A_{base}(1 - f)) + \sigma_{ls}A_{base}R_af + \sigma_{sg}(A_{base}R_a(1 - f) + (A_n - A_{base})R_a) \quad (4)$$

where A_{cap} is the surface area of the top of the drop, which is assumed to be a spherical cap, and is equal to $2A_{base}(1 - \cos \theta)/\sin^2 \theta$. After substituting the expressions for A_{cap} and A_n, and relating the equilibrium contact angle, θ_{eq}, to $\sigma_{ls} - \sigma_{sg}$ through Young's equation[43,49] ($\sigma_{lg}\cos \theta_{eq} = \sigma_{ls} - \sigma_{sg}$), the IFE difference between the two growth modes, $\Delta E = E_{SPOT} - E_{CA}$, is equal to:

$$\Delta E = \sigma_{lg}\bigg(\big(2 - f + R_a f\cos \theta_{eq}\big)$$

$$\bigg(A_{base} + \frac{A_{base}^{3/2}(\cos \theta - 1)^2(2 + \cos \theta)}{3\pi^{1/2}FR_v\sin^3 \theta}\bigg)$$

$$-A_{base}\bigg(f + fR_a\cos \theta_{eq} + \frac{1}{\cos^2 0.5\theta}\bigg)\bigg) \quad (5)$$

Eqn (5) calculates the IFE difference associated with a step increase of the contact angle from 0 to θ. However, during the initial formation stage of the droplet, the contact angle varies continuously, not in a quantized fashion.[33] Thus, to determine how likely it is for a flat wetted spot to begin to grow by contact angle increase, we evaluate how favorable taking such an energetic pathway is. Specifically, we calculate the derivative of eqn (5) with respect to θ at a constant A_{base}:

$$\frac{\partial \Delta E}{\partial \theta} =$$

$$\frac{\sigma_{lg}A_{base}\big(A_{base}^{1/2}(2 - f) + A_{base}^{1/2}fR_a\cos \theta_{eq} - 2\pi^{1/2}FR_v\sin \theta\big)}{4\pi^{1/2}FR_v\cos^4 0.5\theta} \quad (6)$$

and substitute the contact angle for the flat wetted spot ($\theta \approx 0°$) leading to $\sin \theta \approx 0$ and $\cos^4 0.5\theta \approx 1$. We also note that, since we are evaluating the derivative of ΔE at a particular growth stage, the wetting state of the liquid does not change (i.e. the values of F and f are constant). In addition, we assume that $\theta_{eq} \approx 90°$ leading to $\cos \theta_{eq} \approx 0$ because the experimentally measured contact angles for the hydrophobic promoter coatings are in the range of 90° to 100°. Substituting and rearranging we obtain:

$$\left.\frac{\partial \Delta E}{\partial \theta}\right|_{\theta=0} = \frac{\sigma_{lg}A_{base}^{3/2}(2 - f)}{4\pi^{1/2}FR_v} \quad (7)$$

For all superhydrophobic surfaces investigated in this work we found that a minimum confined base area is necessary for the droplet growth to occur through contact angle increase (for example, about 1 μm for drop size distribution in Fig. 1a). The experimental observation of a minimum confined base area suggests that the ΔE needs to increase at some minimum rate for this growth mechanism to be preferred. In other terms, a threshold value of $\partial \Delta E/\partial \theta$ exists, which triggers the confined base area growth. If we assume the threshold value of $\partial \Delta E/\partial \theta$, W, is independent of the surface architecture, we can relate the minimum confined base diameter, $d_m = (4A_{base}/\pi)^{1/2}$, to R_v, F, and f through:

$$d_m = \left(\frac{16FR_v}{\pi\sigma_{lg}(2 - f)}\frac{\partial \Delta E}{\partial \theta}\right)^{1/3} = \left(\frac{16WFR_v}{\pi\sigma_{lg}(2 - f)}\right)^{1/3} \quad (8)$$

Currently, there are no experimental techniques capable of determining the exact wetting state of the condensed microdroplets. To illustrate the effect of the initial wetting state on eqn (8), we model fully wetted (Wenzel), strongly wetted, moderately wetted, and lightly wetted states by setting the value of F to 1, 0.75, 0.35, and 0.15, respectively. As a simplification we assume that, as for vertical nanostructures, f is equal to F for all values of R_v.

To compare the experiments with the derived theory, we measure the initial confined base diameters of twenty-five droplets for each of the investigated surfaces. The three smallest confined base diameters measured for each of the surfaces are plotted as a function of R_v in Fig. 3 (see Experimental section for details of R_v measurement). The value of $W = 0.42$ pJ rad^{-1} $\pm$ 0.03 pJ rad^{-1} is estimated by fitting eqn (8) with $F = 1$ to the d_m data from the 2 NP and 100 nm MaCE surfaces, which are likely to be in nearly fully wetting state.§ This estimated value of W is used in all models. Nearly all experimentally observed d_m values correspond to the theoretical predictions. Only the constant contact angle mode drop growth on the 1 NP surface with an R_v of 101 nm contradicts the theoretical prediction of $d_m \approx 1$ μm. This disagreement results from topographical features on the 1 NP surface that are too gradual and not tall enough for nucleating nanodroplets to form a horizontal interface bridging individual structures.[44] The features need to have vertical side walls for the liquid bridging between the features to occur (ref. 44,47,52 and 53).¶ This requirement is satisfied for most topologies with an aspect ratio greater than one. For example, doubling the number of TMA–water injections (from 1 to 2 injections for the 2 NP surface) increases the density of Al_2O_3 nanoparticles prior to SiO_2 matrix deposition and produces taller and steeper structures. As a result, on the 2 NP surface we begin to see a transition between constant contact angle and constant base area growth modes, with an observable d_m of about 1.6 μm (see Fig. 4g). Surfaces which are fabricated using 4 and 6 TMA–water cycles have even taller and steeper features which support the formation of nearly spherical droplets with d_m values of about 1.4 μm and 1.1 μm, respectively (see Fig. 4c and d). For the NP surfaces the R_v increases about 30 nm with each additional
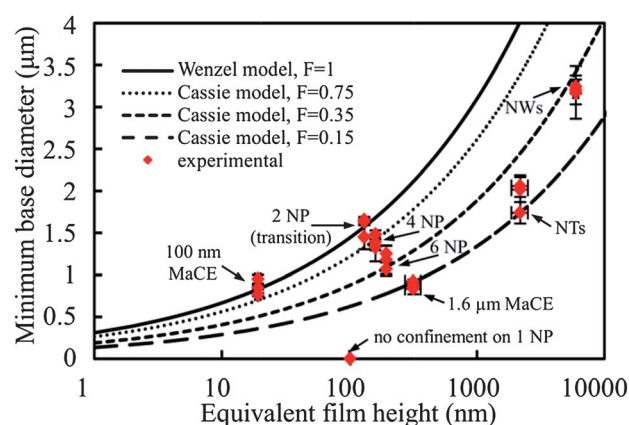

Fig. 3 Comparison of theoretical predictions for Wenzel and Cassie models and the experimentally measured minimum confined base diameters vs. the equivalent film height, R_v, of all investigated surfaces. NP, NW, NT, and MaCE correspond to alumina nanoparticle (preceding number indicates number of TMA–water injections used), silicon nanowire, silicon nanotree, and 100 nm and 1.6 μm thick corrugated silicon surfaces created using MaCE, respectively.

TMA–water injection cycle. The corresponding decrease in d_m indicates that the increase in the height and the aspect ratio of topological features prevents full wetting of the nanostructures during the initial stage of droplet formation (estimated $\approx 75\%$ and $\approx 35\%$ wetting for 4 NP and 6 NP surfaces shown in Fig. 4). In contrast to the gradually varying topography in the series of NP surfaces, the silicon protrusions created using MaCE are nearly vertical,[38–40] and promote wet spot formation for both 100 nm and 1.6 μm etch depths. Both of the MaCE surfaces have a d_m of about 0.9 μm (see Fig. 4a and b), which is a clear indication that droplets forming on the surface with deeper protrusions are in lightly wetted state (following theoretical prediction for $F \approx 0.15$). The surfaces consisting of the 2.6 μm tall DRIE silicon nanotrees (NT) and the 8.4 μm tall VLS silicon nanowires (NW) have R_v of 2.2 μm and 6 μm, and corresponding d_m of about 1.9 μm and 3.2 μm, respectively (see Fig. 4e and f). The nearly spherical droplets forming on the NW surface are in a moderately wetted state (following theoretical prediction for $F \approx 0.35$). The droplets forming on the NT surface are in lightly wetted state, corresponding to $F \approx 0.15$. However, this only shows that drops with the smallest base diameter are in the partially non-wetting states. It is possible that the same surface can exhibit co-existence of microdroplets in both the Wenzel and the Cassie states.[32] We also note that surfaces with R_v greater than about 500 nm‖ can have geometrical features with dimensions or spacing greater than several hundred nanometers, and thus might not retain superhydrophobic characteristics during condensation.

---

§ The drops growing in a confined base mode on the 2 NP surface, on which both the confined and unconfined wetting modes are exhibited, are likely to be in nearly fully wetting state. The drops on the lightly and strongly corrugated silicon surfaces have nearly identical values of d_m, but drastically different values of R_v. Since the primary difference in the topology of these two surfaces is their depth, we assume that the lightly corrugated surface, with a depth below 100 nm, is nearly fully wetted. The fit is calculated using an R statistical data analysis package with a variance weighted least squares method and the reported uncertainty is calculated with a coverage factor of 1.

¶ For the void filling to occur, the surface needs to interact with nucleating water clusters to form a horizontal interface bridging the topological features.[44] The formation of capillary bridges between the nanostructures is highly dependent on the fine structure of the surface architecture.[59] From a purely geometrical perspective, a horizontal liquid interface will form if the sum of the water contact angle and the local surface inclination angle is equal to or greater than 180°. For example, Ruckenstein and Berim[52] showed that a spherical cavity with a radius C on a surface with the equilibrium water contact angle θ_{eq} needs to be at least $C(1 - \cos \theta_{eq})$ deep for the flat interface to form. A similar requirement can be derived from molecular dynamics simulations. For example, Koishi et al.[47] showed that for hydrophobic surfaces with an atomic scale topology, the asperity depth needs to be comparable to the droplet size before liquid can spread between the structures.

‖ Caution should be taken when using equivalent film height as a metric to evaluate wetting properties of structured surfaces with $R_v > R_{nano} \approx 500$ nm. This value represents a conservative estimate for which a surface can have geometrical dimensions greater than several hundred nanometers, for example, in the case of the hypothetical square pillar surface when $L_s = 0.5L = l = H$, $R_v = 0.75\,L_s$. Thus, an R_v of 500 nm represents a surface with $l = 667$ nm and $L = 1334$ nm. Based on previous literature cited in the paper, it is unlikely that such surfaces will have superhydrophobic characteristics when condensed on.
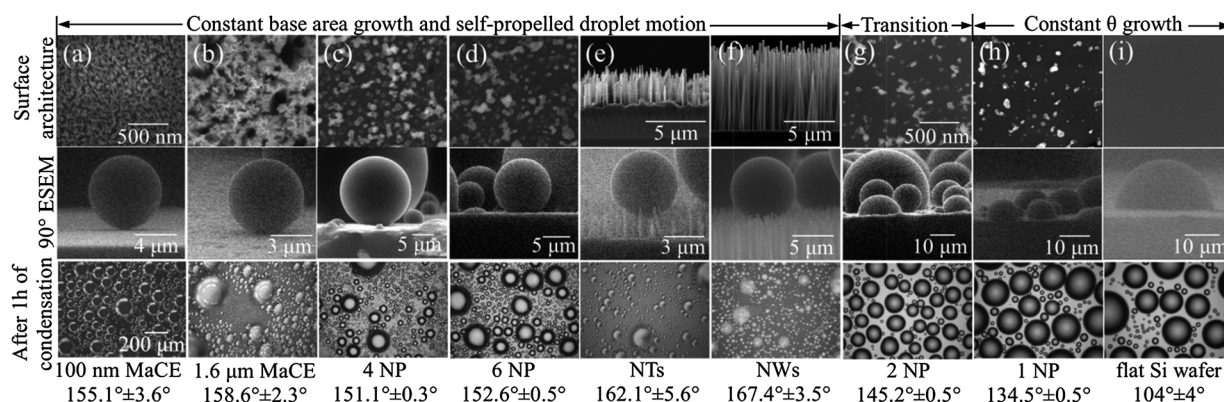
Fig. 4 SEM images of the surface architecture, example side-view ESEM™ images of typical condensed microdroplets, and top down light microscopy images of the surface following one hour of condensation at standard conditions for temperature and pressure with a relative humidity of 30% to 50% and a surface subcooling of $\Delta T \approx 6$ K. Macroscale contact angles are indicated below the surface name.

Lastly, we compare the growth mechanism of individual droplets observed with high magnification ESEM™ to ensemble condensation dynamics observed using low magnification light microscopy. We observe that a coalescence-triggered self-propelled motion of droplets occurs only on surfaces where high contact angle microdroplets form through confined base area growth (see Fig. 4). On surfaces with both growth modes present or only the constant contact angle growth mode present, droplets will not roll off until they reach sizes of a few millimeters when the sample is vertically oriented.[54–56] We do not investigate the relationship between the droplet speed and the surface architecture in this work. The speed of the droplet depends on the surface energy released during coalescence[4,57] and is a non-linear function of R_a.[57] Therefore, we do not necessarily expect a direct correlation between the droplet speed and the value of d_m.

Conclusions

To conclude we answer the question: how nanorough is rough enough to make a surface superhydrophobic during water condensation? We demonstrate that the surface needs to be rough enough to promote formation of capillary bridges between individual features and to energetically confine the created wetted flat spots to diameters significantly lower than the average spacing between individual droplets (about 10 μm).[5,27,32] These requirements are easily satisfied by having topological features with an aspect ratio of at least one and $R_v \leq R_{nano} \approx 500$ nm.‖ For such surfaces the macroscale contact angle is also an indicator of whether or not the surface will be superhydrophobic during condensation (see Fig. 4). In contrast, the macroscale contact angle does not predict the droplet growth mechanism for surfaces with $R_v \gg R_{nano}$, whose wetting properties are determined by dimensions and spacing of their topological features. In terms of a hypothetical periodic square pillar surface (represented schematically in Fig. 2; for such geometry $R_v = H(L^2 - l^2)/L^2$), surfaces with $L \gg l$ and $L \gg R_{nano}$ are too sparse to disrupt condensation dynamics. The Wenzel model predicts that surfaces with $L \gg l$ and $L \leq R_{nano}$, and features sufficiently tall to induce wetted flat spot formation, will have a d_m of several micrometers, and thus are likely to be wetted completely. We schematically

show in Fig. 5 that to display superhydrophobic properties during condensation, surfaces with $R_v \gg R_{nano}$ need to have L and l significantly smaller than R_{nano}. On surfaces which follow the above guidelines, confined base area growth leads to the formation of nearly spherical microdroplets, which is a necessary condition for droplets to become highly mobile after coalescence.

Our theoretical analysis directly links d_m to R_v, F, and f. Limitations imposed by current experimental techniques prevent full validation of our model (with experimentally measured values of F and f). However, with the estimated value of W, our methodology enables a rough estimation of the wetting state below the droplets. With current fabrication techniques it is difficult to make surfaces with significantly higher density of sub-50 nm vertical structures than those achieved through the MaCE process. Therefore, droplets with d_m significantly below 0.8 μm are unlikely to occur. Correspondingly, we estimate a minimum threshold R_v needed for the formation of drops in the Cassie–Baxter state as about 35 nm ($R_v = d_m^3 \pi \sigma_{lg}(2 - f)/(16WF)$ with $f = F = 0.9$). This is important for heat transfer applications, where it is desirable to have drops in a partially wetting state to enhance droplet mobility,[4,23,58] while at the same time minimizing the detrimental thermal resistance of the gas pocket below the drop.[32] The fundamental insight developed in this work provides quantitative guidelines for designing surfaces which manifest superhydrophobic properties during condensation. We also highlight that our methodology relies on the introduced
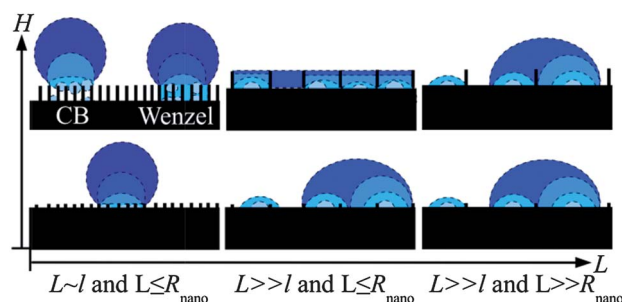
Fig. 5 Summary of influence of L, H, and l on microdroplet condensation growth modes; CB stands for the Cassie–Baxter state.

equivalent film height parameter, which is a universal metric that allows for facile comparison of the arbitrarily complex surface architectures. The established guiding design principles will hopefully enhance the applicability of such coatings.

Experimental

ESEM imaging procedure

Water condensation is imaged using FEI Quanta 200 FEG ESEM™. The sample is mounted at 85° to 90° on a custom-made brass sample holder to prevent electron beam damage to the hydrophobic coating[29] and provide a clear view of the growing droplets.[5,28] The working distance is set to 6 mm to 8 mm. After two purging cycles, the sample is chilled at −10 °C to −15 °C at a vapor pressure of 150 Pa for two minutes. Sustained water condensation is achieved by a step increase in the pressure to about 800 Pa to 900 Pa. Because the water-cooled thermoelectric (Peltier) cooling stage cannot remove all the heat released by the condensation process, the sample temperature quickly increases to the saturation temperature corresponding to the set chamber vapor pressure. To avoid transient effects of the pressure and the temperature equilibration, growth of individual microdroplets taking place a few minutes into the condensation process is imaged. To prevent any electron beam heating effects,[27] the drops are imaged with electron beam energy and current of 10 keV and 0.16 nA, respectively. The dynamics of the condensation process are imaged with 512 pixel by 471 pixel frame sizes and 1 μs dwell time. The corresponding images are saved every 0.2 s.

The ESEM™ images are analyzed using the FIJI image analysis software. We directly measure the base diameter, d_{base}. All reported values are averages of six measurements with associated standard error (corresponds to standard deviation) and reported uncertainties are calculated with a coverage factor of 1.

Optical imaging procedure

The condensation process was also imaged using a Leitz Wetzlar Aristomet optical microscope equipped with a Jenoptik Progres digital camera with a 100× objective. The sample was mounted using Antec Formula 5 Silver Thermal Compound to a 1.2 cm by 1.2 cm Analog Technologies Thermoelectric Cooler module mounted to a 2.5 cm × 5 cm × 5 cm aluminum heat sink. The experiment was performed under standard conditions for temperature and pressure (20 °C and 101.3 kPa) and relative humidity of 30% to 50%, which was continually measured and logged using a Lascar EL-USB-2-LCD logger. The Thermo-electric Cooler module surface temperature was measured using a Fluke thermocouple attached to the surface with the silver thermal compound and electrical tape. Condensation was initiated by quickly decreasing and maintaining the Thermoelectric Cooler module surface temperature at 0.2 °C ± 0.2 °C. For each experiment, 694 by 516 pixel images with 100 ms exposure time and 5 V light bulb voltage were captured every minute over a period of 80 minutes. To provide a 10° tilt angle without defocusing part of the viewing area, one side of the microscope was raised about 8 cm (see Rykaczewski et al.[29] for more information).

Superhydrophobic surface fabrication procedure

The fabrication procedure for the flat hydrophobic silicon and the Al_2O_3 nanoparticle superhydrophobic surfaces is described in depth by Rykaczewski et al.[29] In this work, the Al_2O_3 nanoparticle surfaces were especially designed to gradually vary the nanoparticle surface density. Specifically, the number of trimethylaluminium (TMA) and water vapor ($2Al(CH_3)_3 + 3H_2O \rightarrow Al_2O_3 + 6CH_4$) reaction cycles was varied prior to deposition of a thin SiO_2 encapsulating matrix via Atomic Layer Deposition (ALD). We fabricated surfaces using 1, 2, 4, and 6 injection cycles (these surfaces are referred to as 1 NP, 2 NP, 4 NP, and 6 NP surfaces, respectively). In the final fabrication step, the surface with nanoparticles is modified with a functionalization exposure to tridecafluoro-1,1,2,2-tetrahydrooctyltrichlorosilane (FOTS). To remove any loose nanoparticles, all surfaces were ultrasonicated in ethanol for 1 minute prior to characterization and used in condensation experiments. As in a previous work, all alumina nanoparticle based superhydrophobic surfaces were fabricated using RPX-540 manufactured by Integrated Surface Technologies.[36]

To fabricate the silicon nanotree (NT) surfaces we used a modified Bosch deep reactive ion etching (DRIE) process. The DRIE process includes cyclic passivation and etching modes. A thin film of fluoride polymer was firstly deposited on the solid surface in the passivation cycle, followed by the etching cycle. We carefully tuned the ratio of the etching and passivation time durations to prevent the polymer film from being completely removed. Thus, the residual polymer particles naturally serve as a random nanomask for the consequent etching. As the etching and passivation proceed alternately, the silicon nanopillars are gradually formed. The coil power was set at ∼550 W. The chamber pressure and temperature were kept at ∼25 mTorr and ∼20 °C, respectively. In the passivation cycle, the C_4H_8 flow rate was ∼85 sccm.

In the etching cycle, the SF_6 flow rate was ∼70 sccm and platen power was set at ∼15 W. Nanotrees with a diameter of about 400 nm, pitch of about 700 nm and height of about 2600 nm were formed after 20 processing cycles. All the surfaces were modified by immersion in 1 mM hexane solution of perfluorooctyl trichlorosilane for ∼30 min, followed by heat treatment at ∼150 °C in air for one hour.[42] SEM images of typical nanotrees are shown in Fig. 6.

The silicon nanowires (NW) with diameters between 50 nm and 200 nm and height of about 8.6 μm were grown in a custom-designed horizontal hot-walled chemical vapor deposition (CVD) system at 850 °C using a $SiCl_4$–H_2–N_2 gaseous mixture. The vapor–liquid–solid (VLS) growth was catalyzed by gold nanoparticles formed on a Si(111) substrate by annealing a 5 nm thick gold (Au) film. Further details of the growth can be found elsewhere.[37]

Lastly, to fabricate the lightly and strongly corrugated silicon surfaces, we used metal assisted chemical etching of silicon (MaCE). 3 nm Au films are deposited using a Denton Infinity 22 electron beam evaporator at 400 μPa (3 μTorr) and a 0.1 nm s⁻¹ deposition rate on p-type (8 Ω cm to 12 Ω cm) single crystal (100) silicon wafers that were cleaned using a dilute HF aqueous solution (1 : 10) for 30 seconds prior to deposition. Next the samples were etched in a mixture of 16 mL of HF (Aldrich, 49%),
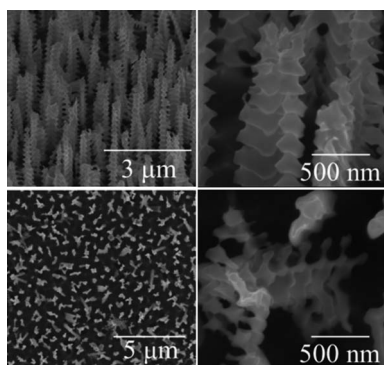
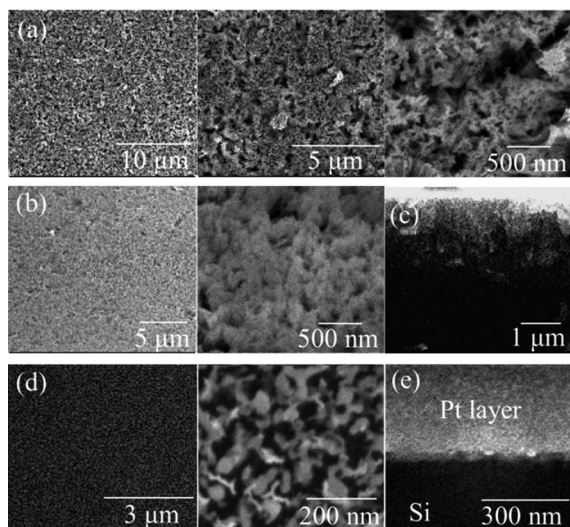**Fig. 6** 52° tilt and top down images of silicon nanotree structures.

Fig. 7 (a) Top down view and (b) 52° view of strongly corrugated silicon (referred to as 1.6 μm MaCE in the paper), (c) side-view of cleaved strongly corrugated silicon, and (d) top down and (e) 52° view of Focus Ion Beam cross-section of lightly corrugated silicon (referred to as 100 nm MaCE in the paper).

4.8 mL of H$_2$O$_2$ (Aldrich, 30%), and 6.8 mL of methanol. A drop of the etchant solution is dispensed onto a sample using a pipette. The samples were etched for a period of 5 s and 120 s to produce the lightly corrugated silicon with a thickness of 98 nm ± 26 nm and the strongly corrugated silicon with a thickness of 1625 nm ± 208 nm, respectively. After etching, the samples are thoroughly rinsed in DI water and dried with nitrogen gas. A hydrophobic monolayer formation on the samples is accomplished by exposure to 1H,1H,2H,2H-perfluorodecyltrichlorosilane (Alfa Aesar) in the desiccator under house vacuum for 24 to 48 hours. Wafers are then rinsed with 2-propanol and dried, yielding the superhydrophobic surfaces. SEM images of resulting surfaces are shown in Fig. 7.

Wetting properties of the utilized surfaces

The static contact angles were measured using a camera-based system (First 10 Angstroms) with a vendor-supplied image capture and analysis software. The reported static contact angles are averages of six goniometer measurements in three locations across the surface; the calculated uncertainty is expressed with a coverage factor of 2.

Surface topography characterization and equivalent film height measurement

The topography of the surfaces was characterized using Atomic Force Microscopy (AFM), Scanning Electron Microscopy (SEM), and Focus Ion Beam (FIB) milling (Table 1). Tapping mode AFM was used to measure the topology of the NP and 100 nm MaCE surface. Drift in this measurement was corrected for by leveling individual traces. The flat regions that are areas of exposed substrate in the NP surfaces were used to fit a line and level the trace, and the unetched peaks were used for the 100 nm MaCE surface. Once the leveled topology was generated, the "fill height", H_{film}, was determined at 98.5% using a cumulative distribution function of the heights. The volume of condensed liquid completely filling the voids between the nanostructures, V_{total}, was estimated from an individual pixel height, H_{pix}, and these two planar surfaces. Unfortunately, it is not possible to determine the contribution of the leveling procedure to the uncertainty of this measurement in a rigorous way; however, the standard deviation of the residuals from the linear fit to the substrate data points was less than 1 nm. Thus, we use 1 nm as the standard error associated with the AFM height measurement, σ_{H-AFM}. The roughness parameter, R_v, for the NP and the 100 nm MaCE surfaces was calculated from the AFM measurements according to:

$$R_{v-AFM} = V_{total}/A_{scan} = \sum_1^{512^2} \frac{(H_{film} - H_{pix})A_{pixel}}{A_{scan}}$$

$$= \sum_1^{512^2} \frac{(H_{film} - H_{pix})A_{pixel}}{512^2 A_{pixel}} = \frac{1}{512^2} \sum_1^{512^2} (H_{film} - H_{pix}) \quad (9)$$

The associated standard error is calculated as $\sigma_{Rv-AFM} = (\sigma_{H-film}^2 + \sigma_{H-pix}^2)^{1/2} = 2^{1/2}\sigma_{H-AFM}$.

Because of their high aspect ratio, the 1.6 μm MaCE, the NT, and the NW surfaces cannot be characterized using AFM. The thickness of the 1.6 μm MaCE surface was determined using FIB cross-sectioning done according to the typical procedure.[40] In the MaCE process, the etched silicon protrusions are a direct imprint of the deposited porous metal film on the surface. Thus, we assume that the planar features of the 100 nm and the 1.6 μm deep MaCE surfaces are identical, and that the thicker surface can be approximated as a further extrusion of the thinner surface. Accordingly, the R_v for the deeper surface is estimated as $R_{v-thick} = R_{v-thin}H_{thick}/H_{thin}$. The associated standard error is calculated according to:

$$\sigma_{R_{v-thick}} = \left(\frac{R_{v-thin}^2 H_{thin}^2 \sigma_{H-thick}^2 + H_{thick}^2 \left(H_{thin}^2 \sigma_{R_{v-thick}}^2 + R_{v-thin}^2 \sigma_{H-thin}^2\right)}{H_{thin}^4} \right)^{1/2}$$

(10)

Table 1 Summary of hydrophobic surface characterization

Surface	CA	σ_{CA}	d_m, μm	σ_{dm}, μm	R_v, nm	σ_{Rv}, nm	H_{film}, nm	σ_{Hfilm}, nm	Method
100 nm MaCE	155.1	3.6	0.86	0.03	19	1.4	95	1.4	AFM
6 NP	151.0	0.3	1.17	0.12	195	1.4	245	1	AFM
4 NP	152.7	0.5	1.40	0.11	160	1.4	195	1	AFM
2 NP	145.2	0.5	1.58	0.07	131	1.4	151	1	AFM
NTs	162.1	5.7	0.94	0.14	2185	321	2587	377	FIB/SEM
1.6 um MaCE	158.7	2.3	0.88	0.04	329	45	1625	208	FIB/SEM
NWs	167.4	3.5	3.21	0.19	5969	292	8425	208	FIB/SEM
1 NP	134.4	0.5	0.00	0.00	101	1.4	117	1	AFM

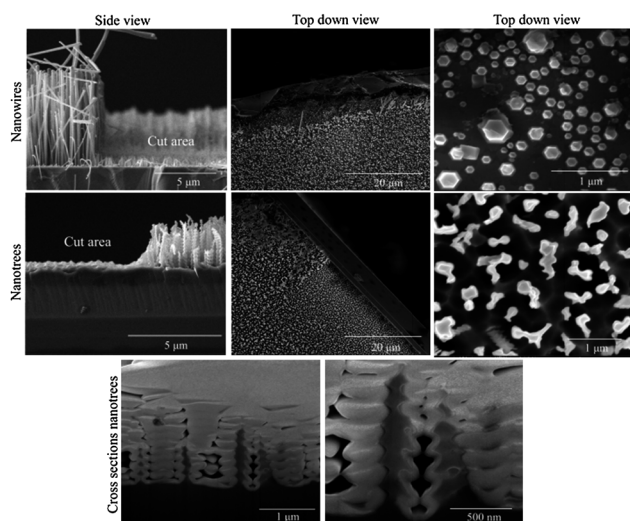For the NW surface we assume that R_v can be calculated as

$$R_{v-NW} = (1 - A_{base-NWs}/A_{base-total})H_{NW} = (1 - G_{NW})H_{NW} \quad (11)$$

In turn, we calculate the R_v for the NT surface as

$$R_{v-NT} = (1 - (A_{base-NTs}/A_{base-total})(A_{x-scalloped}/A_{x-original}))$$
$$H_{NT} = (1 - G_{NT}G_{NT-vertical})H_{NT} \quad (12)$$

where $G_{NT-vertical}$ is a fraction estimating the reduction of the volume of a uniform pillar due to scalloping. This fraction is estimated from vertical FIB cross-sections along the nanotree axis. The base area fractions of the nanowires and the nanotrees, G_{NW} and G_{NT}, were estimated by FIB milling most of the structures off at a 90° and top down imaging of the cut area (see Fig. 8). This area fraction for the NW and NT surfaces was estimated using the particle analysis function in FIJI. The images were thresholded and despeckled prior to analysis. The area fractions and standard errors were estimated by performing the analysis on four images for both the cut NTs and NWs. The standard errors associated with eqn (11) and (12) are calculated as:

$$\sigma_{Rv-NW} = (H_{NW}^2\sigma_{GNW} + (1 - G_{NW})^2\sigma_{HNW}^2)^{1/2} \quad (13)$$

$$\sigma_{R_{v-NT}} = \left((1 - G_{NT}G_{NT-vertical})^2\sigma_{H_{NW}}^2 + G_{NT-vertical}^2H_{NT}^2\sigma_{G_{NW}}^2 \right.$$
$$\left. + G_{NT}^2H_{NT}^2\sigma_{G_{NW-vertical}}^2 \right)^{1/2}$$
$$(14)$$

We obtained values of $G_{NT-vertical} = 0.595 \pm 0.059$, $G_{NW} = 0.276 \pm 0.025$, and $G_{NT} = 0.261 \pm 0.007$. The uncertainties are reported with a coverage factor of 1.

Acknowledgements

Notes and references

1 C. Dietz, K. Rykaczewski, A. G. Fedorov and Y. Joshi, *Appl. Phys. Lett.*, 2010, **97**, 033104.
2 T. Humplik, J. Lee, S. C. O'Hern, B. A. Fellman, M. A. Baig, S. F. Hassan, M. A. Atieh, F. Rahman, T. Laoui, R. Karnik and E. N. Wang, *Nanotechnology*, 2011, **22**, 292001.
3 C. H. Chen, Q. J. Cai, C. L. Tsai, C. L. Chen, G. Y. Xiong, Y. Yu and Z. F. Ren, *Appl. Phys. Lett.*, 2007, **90**, 173108.
4 J. B. Boreyko and C. H. Chen, *Phys. Rev. Lett.*, 2009, **103**, 184501.
5 K. Rykaczewski, J. H. J. Scott, S. Rajauria, J. Chinn, A. M. Chinn and W. Jones, *Soft Matter*, 2011, **7**, 8749–8752.
6 X. Chen, J. Wu, R. Ma, M. Hua, N. Koratkar, S. Yao and Z. Wang, *Adv. Funct. Mater.*, 2011, **21**, 4617–4623.
7 A. Lafuma and D. Quere, *Nat. Mater.*, 2003, **2**, 457–460.
8 C. Dorrer and J. Ruhe, *Langmuir*, 2007, **23**, 3820–3824.
9 C. Dorrer and J. Ruhe, *Langmuir*, 2007, **23**, 3179–3183.
10 K. A. Wier and T. J. McCarthy, *Langmuir*, 2006, **22**, 2433–2436.
11 R. D. Narhe and D. A. Beysens, *Europhys. Lett.*, 2006, **75**, 98–104.
12 R. D. Narhe, W. González-Viñas and D. A. Beysens, *Appl. Surf. Sci.*, 2011, **256**, 4930–4933.

Fig. 8 Side, top down, and cross-sectional images of FIB cut NW and NT structures.

13 R. D. Narhe and D. A. Beysens, *Langmuir*, 2007, **23**, 6486–6489.

14 R. D. Narhe and D. A. Beysens, *Phys. Rev. Lett.*, 2004, **93**, 076103.

15 Y.-T. Cheng and D. E. Rodak, *Appl. Phys. Lett.*, 2005, **86**, 144101.

16 Y. C. Jung and B. Bhushan, *J. Microsc.*, 2008, **229**, 127–140.

17 M. Nosonovsky and B. Bhushan, *Langmuir*, 2007, **24**, 1525–1533.

18 M. Nosonovsky and B. Bhushan, *Nano Lett.*, 2007, **7**, 2633–2637.

19 M. He, J. Wang, H. Li and Y. Song, *Soft Matter*, 2011, **7**, 3993–4000.

20 C. Dorrer and J. Ruhe, *Soft Matter*, 2009, **5**, 51–61.

21 B. Mockenhaupt, H.-J. Ensikat, M. Spaeth and W. Barthlott, *Langmuir*, 2008, **24**, 13591–13597.

22 Y. M. Zheng, D. Han, J. Zhai and L. Jiang, *Appl. Phys. Lett.*, 2008, **92**, 084106.

23 J. B. Boreyko and C. H. Chen, *Phys. Rev. Lett.*, 2009, **103**, 174502.

24 C. Dorrer and J. Ruhe, *Adv. Mater.*, 2008, **20**, 159–163.

25 K. K. S. Lau, J. Bico, K. B. K. Teo, M. Chhowalla, G. A. J. Amaratunga, W. I. Milne, G. H. McKinley and K. K. Gleason, *Nano Lett.*, 2003, **3**, 1701–1705.

26 Q. Ke, S. Zhang, T. Tang, S. Wang and H. Jing, *Colloids Surf., A*, 2011, **377**, 110–114.

27 K. Rykaczewski, J. H. J. Scott and A. G. Fedorov, *Appl. Phys. Lett.*, 2011, **98**, 093106.

28 K. Rykaczewski and J. H. J. Scott, *ACS Nano*, 2011, **5**, 5926–5968.

29 K. Rykaczewski, J. Chinn, M. L. Walker, J. H. J. Scott, A. Chinn and W. Jones, *ACS Nano*, 2011, **5**, 9746–9754.

30 J. B. Boreyko, Y. Zhao and C.-H. Chen, *Appl. Phys. Lett.*, 2011, **99**, 234105.

31 I. Badge, S. Sethi and A. Dhinojwala, *Langmuir*, 2011, **27**, 14276–14731.

32 N. Miljkovic, R. Enright and E. Wang, *ACS Nano*, 2012, **6**, 1776–1785.

33 K. Rykaczewski, *Langmuir*, 2012, **28**, 7720–7729.

34 N. A. Patankar, *Soft Matter*, 2010, **6**, 1613–1620.

35 S. Anand and S. Y. Son, *Langmuir*, 2010, **26**, 17100–17110.

36 J. Chinn, F. Helmrich, R. Guenther, M. Wiltse, K. Hurst and R. W. Ashurst, in *NSTI-Nanotech 2010*, 2010, vol. 1.

37 S. Krylyuk, A. V. Davydov and I. Levin, *ACS Nano*, 2010, **5**, 656–664.

38 Z. Huang, N. Geyer, P. Werner, J. de Boor and U. Gösele, *Adv. Mater.*, 2010, **23**, 285–308.

39 K. Rykaczewski, O. J. Hildreth, D. Kulkarni, M. R. Henry, S. K. Kim, C. P. Wong, V. V. Tsukruk and A. G. Fedorov, *ACS Appl. Mater. Interfaces*, 2010, **2**, 969–973.

40 K. Rykaczewski, O. J. Hildreth, C. P. Wong, A. G. Fedorov and J. H. J. Scott, *Nano Lett.*, 2011, **11**, 2369–2374.

41 Y. Xiu, L. Zhu, D. W. Hess and C. P. Wong, *Nano Lett.*, 2007, **7**, 3388–3393.

42 C.-H. Choi and C.-J. Kim, *Nanotechnology*, 2006, **17**, 5326.

43 V. P. Carey, *Liquid-Vapor Phase-Change Phenomena*, Taylor and Francis, New York, 2nd edn, 2008.

44 J. N. Israelachvili, *Intermolecular and Surface Forces*, Elsevier, San Diego, 3rd edn, 2011.

45 R. N. Wenzel, *Ind. Eng. Chem.*, 1936, **28**, 988–994.

46 A. B. D. Cassie and S. Baxter, *Trans. Faraday Soc.*, 1944, **40**, 546–551.

47 T. Koishi, K. Yasuoka, S. Fujikawa, T. Ebisuzaki and X. C. Zeng, *Proc. Natl. Acad. Sci. U. S. A.*, 2009, **106**, 8435–8440.

48 K. K. Varanasi, M. Hsu, N. Bhate, W. Yang and T. Deng, *Appl. Phys. Lett.*, 2009, **95**, 094101.

49 T. Liu, W. Sun, X. Sun and H. Ai, *Langmuir*, 2010, **26**, 14835–14841.

50 H. H. Liu, H. Y. Zhang and W. Li, *Langmuir*, 2011, **27**, 6260–6267.

51 H. Mayama and Y. Nonomura, *Langmuir*, 2011, **27**, 3550–3560.

52 E. Ruckenstein and G. O. Berim, *J. Colloid Interface Sci.*, 2010, **351**, 277–282.

53 G. O. Berim and E. Ruckenstein, *J. Colloid Interface Sci.*, 2011, **359**, 304–310.

54 J. W. Rose, *Int. J. Heat Mass Transfer*, 1967, **10**, 755–765.

55 E. J. Lefevre and J. W. Rose, *Proceedings of 3rd International Heat Transfer Conference*, Chicago, 1966.

56 J. W. Rose, *Proc. Inst. Mech. Eng., Part A*, 2002, **216**, 115–128.

57 F.-C. Wang, F. Yang and Y.-P. Zhao, *Appl. Phys. Lett.*, 2011, **98**, 053112.

58 J. B. Boreyko, C. H. Baker, C. R. Poley and C.-H. Chen, *Langmuir*, 2011, **27**, 7502–7509.

59 S. Yang, H. Zhang, M. Nosonovsky and K.-H. Chung, *Langmuir*, 2008, **24**, 743–748.